Space Weather

RESEARCH ARTICLE
10.1029/2025SW004354

Key Points:

- Field-aligned current (FAC) intensities increase during high-intensity long-duration continuous auroral electrojet activity (HILDCAA) compared to their pre-HILDCAA values, without significant day-night asymmetry in any particular season
- Both dayside and nightside FAC intensities exhibit prominent seasonal variations during HILDCAAs and pre-HILDCAA quiet intervals

Correspondence to:
R. Hajra,
rhajra@ustc.edu.cn;
rajkumarhajra@yahoo.co.in

Citation:
Hajra, R., Tsurutani, B. T., Lu, Q., & Du, A. (2025). Field-aligned currents during high-intensity long-duration continuous auroral electrojet activity events: Seasonal dependences. *Space Weather*, *23*, e2025SW004354. https://doi.org/10.1029/2025SW004354

Received 16 JAN 2025
Accepted 27 OCT 2025

Author Contributions:
Conceptualization: Rajkumar Hajra, Bruce T. Tsurutani
Data curation: Rajkumar Hajra
Formal analysis: Rajkumar Hajra
Funding acquisition: Rajkumar Hajra
Investigation: Rajkumar Hajra
Methodology: Rajkumar Hajra
Resources: Rajkumar Hajra
Supervision: Bruce T. Tsurutani
Validation: Rajkumar Hajra
Visualization: Rajkumar Hajra
Writing – original draft: Rajkumar Hajra
Writing – review & editing: Rajkumar Hajra, Bruce T. Tsurutani, Quanming Lu, Aimin Du

Field-Aligned Currents During High-Intensity Long-Duration Continuous Auroral Electrojet Activity Events: Seasonal Dependences

Rajkumar Hajra[1], **Bruce T. Tsurutani**[3], **Quanming Lu**[1], **and Aimin Du**[2]

[1]CAS Key Laboratory of Geospace Environment, School of Earth and Space Sciences, University of Science and Technology of China, Hefei, China, [2]College of Earth and Planetary Sciences, Chinese Academy of Sciences, Beijing, China, [3]Retired, Pasadena, CA, USA

Abstract

High-intensity long-duration continuous auroral electrojet activity (HILDCAA) events caused by interplanetary Alfvén waves are associated with global-scale convection events. HILDCAAs occur primarily during the solar cycle declining phase (Hajra et al., 2013, https://doi.org/10.1002/jgra.50530). A statistical study is conducted for 42 HILDCAAs occurring between 2009 and 2023 to investigate associated auroral region field-aligned currents (FACs). The FAC measurements used in this study were made by the Active Magnetosphere and Planetary Electrodynamics Response Experiment. It is shown that HILDCAA-related FAC probability distributions are characterized by a median FAC intensity of ~5 MA, ~2 times the quiet time FAC intensity, with slight variations between day and night, and from one season to the other. During HILDCAAs (pre-HILDCAA quiet times), the dayside FAC intensity is found to be the strongest during summer, ~15%–32% (~92%–96%) stronger than during equinoxes, and ~87% (~128%) stronger than during winter. The nightside HILDCAA-related FAC intensity during fall is found to be ~8%, ~10%, and ~29% stronger than during summer, spring, and winter, respectively. For pre-HILDCAA intervals, the nightside FAC intensity during summer is ~51%, ~62%, and ~94% stronger than during fall, winter, and spring, respectively. These latter results are in clear contrasts to previous results showing no seasonal dependences of nightside FAC intensities during geomagnetic quiet and disturbed times.

Plain Language Summary

High-intensity long-duration continuous auroral electrojet activity (HILDCAA) events are associated with substorms and convection events continuing for days to weeks. HILDCAAs occur primarily in the solar cycle declining phase (Hajra et al., 2013, https://doi.org/10.1002/jgra.50530). The substorms and convection events during HILDCAAs lead to strong currents flowing in the auroral region along the geomagnetic field lines. In the present work, we utilized long-term measurements of these field-aligned current (FAC) intensities to develop their probability distribution functions during HILDCAAs and quiet periods. We show that both dayside and nightside FAC intensities during HILDCAA events exhibit significant seasonal dependences. Seasonal dependences of nightside FACs are in clear contrasts to previous results showing no seasonal dependences of nightside FAC intensities during geomagnetic quiet and disturbed times.

1. Introduction

Geomagnetic field-aligned currents (FACs; Birkeland, 1908, 1913; Zmuda et al., 1966) play an important role in electrodynamical coupling between the magnetosphere and polar ionosphere. They consist of two components: the poleward component or the region 1 current flows into (away from) the ionosphere on the dawnside (duskside); while the equatorward component called the region 2 current connecting to the partial ring current in the inner magnetosphere has opposite polarity (Clausen et al., 2012; Cowley, 2000; Iijima & Potemra, 1976, 1978). Geomagnetic disturbances lead to a strengthening of the FAC intensity and an expansion of their latitudinal width. Region 1 and 2 components are reported to increase during the substorm expansion phase by ~1 MA (e.g., Coxon et al., 2014; Forsyth et al., 2018; Iijima & Potemra, 1978; Käki et al., 2022). Geomagnetic storms are shown to cause FAC enhancements, maximizing during the storm main phase, by up to a factor of ~10 compared to the quiet time nominal FAC intensities (Hajra, Tsurutani, Lakhina, et al., 2024; Hajra, Tsurutani, Lu, Horne, et al., 2024; Knipp et al., 2014; Le et al., 2016; Lyons et al., 2016; Pedersen et al., 2021, 2022; Wang et al., 2006, 2024; Wilder et al., 2012). Recently, Hajra et al. (2025b) reported a ~5 factor increase in the peak

FAC intensity during high-intensity long-duration continuous auroral electrojet (AE) activity (HILDCAA; Tsurutani & Gonzalez, 1987) events, caused by interplanetary Alfvén waves, primarily during the solar cycle declining phase (Hajra et al., 2013).

Previous case studies have reported an asymmetry in dayside FAC intensity between summer and winter hemispheres (Wang et al., 2006), while similar FAC intensifications in spring and fall hemispheres (Anderson et al., 2002) during intense geomagnetic storms. Statistical studies by Fujii et al. (1981) and Coxon et al. (2016), without considering geomagnetic conditions, reported that dayside FAC intensities in the summer hemisphere are ~2 times the winter hemispheric FAC intensities. All these studies found that nightside FACs do not exhibit such seasonal dependences. Recently, Hajra et al. (2025a) studied long-term trends in FAC intensities based on ~15 years of FAC measurements by the Active Magnetosphere and Planetary Electrodynamics Response Experiment (AMPERE; Waters et al., 2001, 2020; Anderson et al., 2002, 2021). They reported significant seasonal dependences both of dayside and nightside FAC intensities, independent of solar activity levels. While FAC statistical (quiet time) features (e.g., Cheng et al., 2018; Coxon et al., 2016; Fujii et al., 1981; Hajra et al., 2025a; Laundal et al., 2018; Qu et al., 2024; Wang et al., 2024; Wang & Lühr, 2023), their variations during geomagnetic storms and substorms are studied previously (see references above), less understood are the FAC variations during HILDCAAs (e.g., Hajra et al., 2025b).

Here we expand on the Hajra et al. (2025b) work to study the seasonal distributions of HILDCAA-related FAC intensities using a long-term database. Seasonal variations of HILDCAA-related FAC intensities will be compared with those during isolated substorms and magnetic storms. This study is aimed at increasing our understanding of FACs during geomagnetic disturbances, helpful for developing FAC prediction model.

2. Data and Methods

2.1. Data

The radial FAC intensity I_r time series (at 2-min cadence over a 10-min window) is obtained from the AMPERE Science Data Center of the Johns Hopkins Applied Physics Laboratory. The currents are derived from the magnetic field perturbations $\delta\boldsymbol{B}$ measured by the Iridium® Communications constellations of about 70 polar satellites at 780 km altitude (Anderson et al., 2002, 2021; Waters et al., 2001, 2020). The near-Earth (at the Earth's bow shock nose) solar wind plasma and interplanetary magnetic field (IMF) data (1-min) are obtained from NASA's OMNIWeb Plus database (King & Papitashvili, 2020). The IMFs are in the geocentric solar magnetospheric coordinates, where x-axis is directed toward the sun, the y-axis is in the $\boldsymbol{\Omega} \times \hat{\boldsymbol{x}}/|\boldsymbol{\Omega} \times \hat{\boldsymbol{x}}|$-direction, where $\boldsymbol{\Omega}$ is aligned with the geomagnetic south pole, and the z-axis completes a right-hand system.

The 1-min geomagnetic ring current (Dessler & Parker, 1959; Sckopke, 1966) index SYM-H (Iyemori, 1990) is obtained from the World Data Center for Geomagnetism, Kyoto, Japan. The 1-min auroral indices (Rostoker, 1972), SME and SML, are obtained from the SuperMAG database (Gjerloev, 2009, 2012; Newell & Gjerloev, 2011a, 2011b). The SME index is equivalent to traditional auroral electrojet index AE (see below), and SML represents the westward component of the auroral electrojet current.

2.2. Methods

The HILDCAA events studied in this work are obtained from Hajra et al. (2025b). The events are identified using the "classical" HILDCAA criteria (Tsurutani & Gonzalez, 1987): (a) the peak AE ≥1,000 nT, (b) the event duration ≥2 days, (c) AE not falling below 200 nT for >2 hr at a time, and (d) the ring current index Dst >−50 nT during the event (note that in this work, we have replaced twelve magnetometer-based AE index by hundreds of magnetometer-based SME, and 1-hr Dst index by 1-min SYM-H index). See Hajra et al. (2025b) for a detail description of the HILDCAA identification method.

For the present analyses, we have used FAC intensities I_r obtained from integrated AMPERE current density J_r distributions (see Anderson et al., 2014, 2021 for detail method). Using integrated current I_r upward and downward components, we computed total integrated currents flowing in the Birkeland system, estimated as $(\mathrm{FAC_{up}} - \mathrm{FAC_{down}})/2$, where $\mathrm{FAC_{up}}$ and $\mathrm{FAC_{down}}$ are the upward and downward components of the FACs, respectively (Anderson et al., 2021). As $\mathrm{FAC_{up}}$ is a positive quantity and $\mathrm{FAC_{down}}$ is a negative quantity, total current defined above is a positive quantity. The current has been separated in dayside and nightside components,

FAC_{day} and FAC_{night}, respectively. The dayside and nightside FAC intensity integrations refer to 06–18 magnetic local time (MLT) and 18–06 MLT (through midnight), respectively, in Altitude Adjusted Corrected Geomagnetic Coordinate (AACGM; Baker & Wing, 1989) local time. We have also computed total current: $FAC_{total} = FAC_{day} + FAC_{night}$. To compute probability distribution functions (PDFs) of FAC intensities, the minimum-to-maximum FAC intensity range is divided into 0.25-MA bins, and FAC observation numbers are counted for each bin. They are then expressed as percentages of total observation counts.

The statistical difference of two distributions is verified by two-tailed probability factor or p-value (Reiff, 1990). For distributions that may not be normal, nonparametric Mann Whitney Wilcoxon test/Mann Whitney U test/Wilcoxon Rank Sum test (Gibbons & Chakraborti, 2011) is used for the p-value computation to compare the median values of the distributions (see Appendix A for details). A p-value less than 0.05 suggests that the two medians are significantly (statistically) different from each other (Press et al., 1992).

We conducted "double superposed epoch analyses" to identify mean variations of FAC intensities during HILDCAAs. In this process, FAC intensity variations are first organized by the HILDCAA onset times (considered as the zero epoch time). Then, the individual HILDCAA duration is normalized by the mean HILDCAA duration. This second step is used to avoid overlapping/averaging of FAC intensities during HILDCAAs and after-HILDCAA quiet intervals, for HILDCAAs with varying durations.

3. Results

3.1. Case Studies

Figure 1 shows examples of FAC intensity variations associated with two HILDCAAs, during 10–12 December 2015 (left panels) and during 21–23 March 2017 (right panels). We describe below the geomagnetic characteristics and the solar/interplanetary causes of the HILDCAAs, and associated FAC intensity variations.

The 2015 HILDCAA initiated at 00:11 UT on 10 December and continued for ∼2.94 days up to 22:43 UT on 12 December (marked by a horizontal red bar, Figure 1g). It is characterized by a peak SME of 1,611 nT. The 2017 HILDCAA had a total duration of ∼2.26 days, from 04:22 UT on 21 March to 10:37 UT on 23 March, with a characteristic SME intensity of 1,490 nT (Figure 1h). During the HILDCAA intervals, SME did not fall below 200 nT for more than 2 hr at a time, and the SYM-H peak intensities were −19 and −46 nT, respectively (Figures 1e and 1f), indicating only weak ring current activity. Negative episodes of SML indicate strong substorm activity during the HILDCAAs (Figures 1i and 1j). However, they were significantly weaker than a supersubstorm (SSS) characterized by an SML peak intensity ≤−2,500 nT (Hajra et al., 2016, 2023; Hajra & Tsurutani, 2018; Tsurutani et al., 2015; Tsurutani & Hajra, 2023).

The 2015 HILDCAA onset is associated with an interaction between a solar wind slow stream with a proton speed V_p of ∼430 km s^{-1} on 9 December and a high-speed stream (HSS; Neugebauer & Snyder, 1966; Phillips et al., 1995; Tsurutani et al., 2006) with V_p of ∼550–700 km s^{-1} on 10–12 December (Figure 1a). The HSS was emanated from a coronal hole located at the solar equator (Krieger et al., 1973). The interaction region is characterized by compressed plasma and IMF, a proton density N_p peak of ∼15 cm^{-3} (Figure 1a), an IMF magnitude B_0 peak of ∼12 nT (Figure 1c), representing a corotating interaction region (CIR; Smith & Wolfe, 1976). The CIR is marked by a vertical gray shading. For the 2017 HILDCAA event, the CIR between a V_p ∼315 km s^{-1} slow stream (on 20 March) and a V_p ∼500–720 km s^{-1} HSS (on 21–24 March; Figure 1b) is characterized by a peak N_p of ∼53 cm^{-3} (Figure 1b), and a peak B_0 of ∼19 nT (Figure 1d). The IMF B_z component is largely fluctuating between northward and southward directions during the CIRs and HSSs (Figures 1e and 1f). These fluctuations are interplanetary Alfvén waves (Alfvén, 1942; Belcher & Davis, 1971; Coleman, 1966; Neugebauer et al., 1984). These solar wind plasma and IMF variations indicate typical solar wind/interplanetary behavior during HILDCAAs (more examples may be found in Tsurutani and Gonzalez (1987), Tsurutani et al. (2006), Hajra et al. (2013, 2014a, 2014b, 2014c), Hajra, Tsurutani, Echer, Gonzalez, Brum, et al. (2015), Hajra, Tsurutani, Echer, Gonzalez, & Santolik (2015), Hajra et al. (2020), Hajra, Tsurutani, Lu, Lakhina, et al. (2024), Hajra (2021)).

Figures 1k–1n show the dayside and nightside FAC intensities FAC_{day} and FAC_{night}, respectively, flowing in the northern and southern hemispheres during the HILDCAAs. The 2015 and 2017 HILDCAAs correspond to northern (southern) hemispheric winter (summer) and spring (fall) seasons, respectively. The HILDCAA events, in general, are characterized by enhanced FACs compared to the pre-HILDCAA and post-HILDCAA FAC

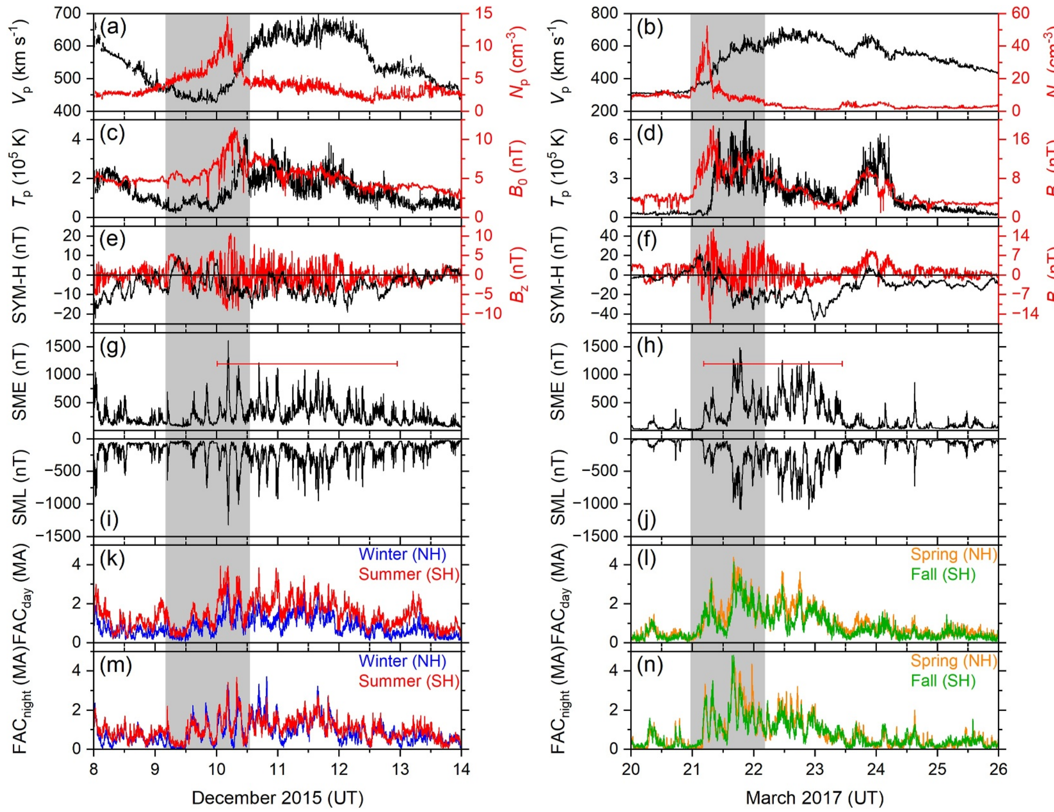

Figure 1. Solar wind parameters, geomagnetic indices, and field-aligned current (FAC) intensity variations during two high-intensity long-duration continuous auroral electrojet (AE) activity (HILDCAA) intervals. From top to bottom, the panels show (a), (b) solar wind proton speed V_p (black, legend on the left) and proton density N_p (red, legend on the right), (c), (d) proton temperature T_p (black, legend on the left) and interplanetary magnetic field (IMF) magnitude B_0 (red, legend on the right), (e), (f) symmetric ring current index SYM-H (black, legend on the left) and IMF B_z (red, legend on the right), (g), (h) auroral electrojet index SME, (i), (j) auroral electrojet index westward component SML, (k, l) dayside FAC (FAC_{day}) intensities, and (m, n) nightside FAC (FAC_{night}) intensities. Left and right panels correspond to the HILDCAA events occurring during 10–12 December 2015 and during 21–23 March 2017, respectively. In panels (k)–(n), different colors correspond to the northern hemispheric winter (blue), southern hemispheric summer (red), northern hemispheric spring (orange), and southern hemispheric fall (green) seasons. Vertical gray shadings indicate the corotating interaction region (CIR) intervals. Horizontal red bars in panels (g) and (h) indicate the HILDCAA intervals.

intensities. For the 2015 event, the nightside FACs are comparable between summer and winter hemispheres (Figure 1m), while the dayside FACs are prominently stronger in the summer hemisphere than in the winter hemisphere (Figure 1k). For the 2017 event, there is no significant difference in the FAC intensities between the spring and fall hemispheres (Figures 1l and 1n).

3.2. Statistical Results

Hajra et al. (2025b) identified 42 HILDCAAs occurring between October 2009 and December 2023, with suitable AMPERE FAC measurements in both hemispheres. We considered FAC measurements during each of the 42 HILDCAAs, and a ∼2-day interval characterized by SYM-H >−50 nT and SME <500 nT prior to the HILDCAA onset, the latter being defined as a quiet interval. Figures 2a–2c show distributions of the HILDCAA-related and quiet (pre-HILDCAA) total FAC intensity (FAC_{total}), dayside FAC intensity (FAC_{day}), and nightside FAC intensity (FAC_{night}), respectively. The statistical results are summarized in Table 1. Here, FAC_{day} (FAC_{night}) represents total dayside (nightside) integrated FAC intensity computed by adding measurements in both hemispheres. Adding measurements from both hemispheres effectively removes any seasonal influence on FACs (e.g., Anderson et al., 2021).

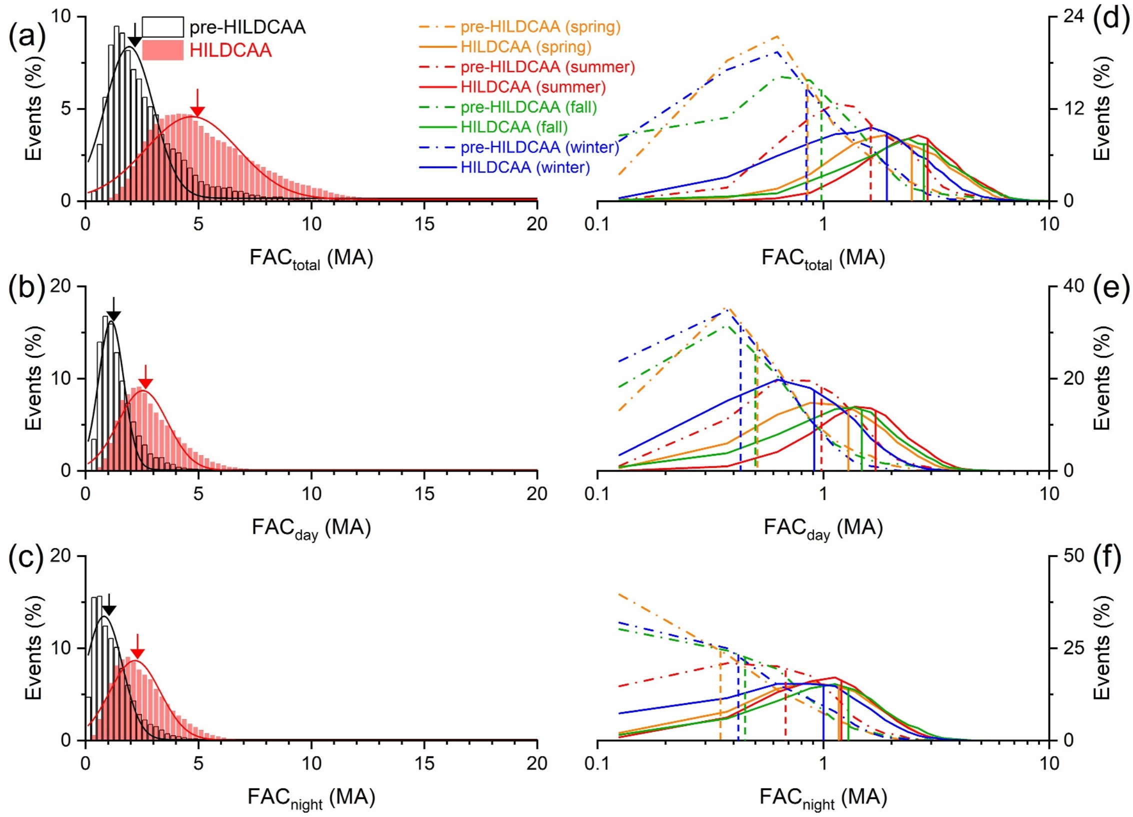

Figure 2. Distributions of (a), (d) FAC$_{total}$ intensity, (b), (e) FAC$_{day}$ intensity, and (c), (f) FAC$_{night}$ intensity for both hemispheres combined (left panels) and for spring (orange), summer (red), fall (green), and winter (blue) hemispheric FAC measurements (right panels). Distributions for HILDCAAs (pre-HILDCAA intervals) are shown by red histograms (empty histograms) in the left panels, and by solid lines (dash-dot lines) in the right panels. Median FAC intensities are marked by downward arrows (vertical lines) in the left panels (right panels).

FAC intensities exhibit large ranges of variations during the HILDCAAs and quiet intervals, as clear from large values of the estimated 1-σ deviations (Table 1). During quiet intervals, the 1-σ deviations are ~66% of the mean intensities for FAC$_{total}$, ~61% for FAC$_{day}$, and ~75% for FAC$_{night}$. For HILDCAA-related FACs, the deviations are comparatively lower, ~45%, ~45% and ~51% for FAC$_{total}$, FAC$_{day}$ and FAC$_{night}$, respectively.

In general, the FAC$_{day}$ intensities (Figure 2b) are stronger than the FAC$_{night}$ intensities (Figure 2c) during both quiet periods and HILDCAAs; and HILDCAA-related FACs are stronger than quiet time FACs (Table 1). Are these results statistically significant? Statistical significance of the results are verified by computed p-values, and summarized in Table 2. Based on the p-values <0.05, it is concluded that the FAC$_{day}$ intensities are ~20% and ~15% stronger than the FAC$_{night}$ intensities during quiet times and HILDCAAs, respectively. On the other hand,

Table 1
Statistical Mean ±1-σ Deviation (Median) of FAC Intensity Distributions During HILDCAAs and Pre-HILDCAA Quiet Intervals

	Pre-HILDCAA (MA)			HILDCAA (MA)		
	FAC$_{total}$	FAC$_{day}$	FAC$_{night}$	FAC$_{total}$	FAC$_{day}$	FAC$_{night}$
All	2.7 ± 1.8 (2.2)	1.5 ± 0.9 (1.2)	1.3 ± 1.0 (1.0)	5.4 ± 2.5 (5.0)	2.9 ± 1.3 (2.7)	2.5 ± 1.3 (2.3)
Spring	1.2 ± 0.9 (0.9)	0.7 ± 0.5 (0.5)	0.5 ± 0.5 (0.4)	2.7 ± 1.3 (2.5)	1.4 ± 0.7 (1.3)	1.3 ± 0.7 (1.2)
Summer	1.8 ± 1.0 (1.6)	1.1 ± 0.6 (1.0)	0.8 ± 0.5 (0.7)	3.1 ± 1.3 (2.9)	1.8 ± 0.8 (1.7)	1.3 ± 0.6 (1.2)
Fall	1.3 ± 1.1 (1.0)	0.7 ± 0.6 (0.5)	0.6 ± 0.5 (0.5)	3.0 ± 1.5 (2.8)	1.6 ± 0.8 (1.5)	1.4 ± 0.8 (1.3)
Winter	1.1 ± 0.8 (0.8)	0.5 ± 0.4 (0.4)	0.6 ± 0.5 (0.4)	2.1 ± 1.2 (1.9)	1.0 ± 0.6 (0.9)	1.1 ± 0.7 (1.0)

Table 2
Statistical p-Values Based on Total FAC Intensity Comparisons Shown in Figures 2a–2c and Table 1

		p-value	Inference[a]
FAC_{day} versus FAC_{night}	Pre-HILDCAA	0.00e + 00	FAC_{day} is ~20% stronger than FAC_{night}.
	HILDCAA	0.00e + 00	FAC_{day} is ~15% stronger than FAC_{night}.
Pre-HILDCAA versus HILDCAA	FAC_{total}	0.00e + 00	HILDCAA-related FAC_{total} is ~127% (a factor of ~2.3) stronger than that during quiet times.
	FAC_{day}	0.00e + 00	HILDCAA-related FAC_{day} is ~114% (a factor of ~2.1) stronger than that during quiet times.
	FAC_{night}	0.00e + 00	HILDCAA-related FAC_{night} is ~123% (a factor of ~2.2) stronger than that during quiet times.

Note. A p-value less than 0.05 ($p < 0.05$) indicates statistically significant differences in median values between the two comparing events such as day and night or pre-HILDCAA and HILDCAA intervals. [a]The percentages are based on mean values listed in Table 1.

FAC intensities estimated during HILDCAAs are >2 factor (>100%) stronger than their nominal quiet time values, based on medians of all FAC measurements.

As clear from Figures 2a–2c, the FAC intensities exhibit asymmetric Gauss distributions. Thus, Gauss distribution functions were fitted to the FAC intensity PDFs (percentage) using the Levenberg Marquardt iteration algorithm. The fitted distribution functions are of the following form:

$$P_{\mathrm{FAC}} = P_{\mathrm{FAC}_0} + \frac{A_{\mathrm{FAC}}}{w_{\mathrm{FAC}}\sqrt{\frac{\pi}{2}}} e^{-2\left(\frac{\mathrm{FAC}-x_{c\mathrm{FAC}}}{w_{\mathrm{FAC}}}\right)^2}$$

The Gauss distribution fittings are shown in Figures 2a–2c by solid curves, and the fitting parameters are listed in Table 3. In the distribution functions, the parameter P_{FAC0} is an "offset", $x_{c\mathrm{FAC}}$ ("center") is the central position of the distribution, w_{FAC} is the "width" of the fitted function, and A_{FAC} is the "area" (see Appendix B for further details of the Gaussian distribution function fitting). It may be noted that the HILDCAA-related FAC distributions are shifted to higher FAC intensities with peaks ($x_{c\mathrm{FAC}}$) around 4.7, 2.5, and 2.2 MA for FAC_{total}, FAC_{day}, and FAC_{night}, respectively, compared to peaks around 1.9, 1.1, and 0.8 MA, respectively, for the quiet intervals.

3.3. Seasonal Dependences

The HILDCAA-related and quiet time FAC intensity measurements are separated for spring, summer, fall, and winter hemispheric measurements. Thus, 9 HILDCAAs occurring during northern (southern) hemispheric spring (fall), 16 HILDCAAs occurring during northern (southern) hemispheric summer (winter), 11 HILDCAAs occurring during northern (southern) hemispheric fall (spring), and 6 HILDCAAs occurring during northern (southern) hemispheric winter (summer) seasons correspond to 20 spring and 20 fall HILDCAA-related FAC measurements, 22 summer and 22 winter HILDCAA-related FAC measurements, and equal numbers of pre-HILDCAA FAC measurements in different seasons (Hajra et al., 2025b). The HILDCAA-related and quiet

Table 3
Parameters of the Gauss Probability Distribution Functions Fitted to FAC Intensity Distributions Shown in Figures 2a–2c

	FAC_{total}		FAC_{day}		FAC_{night}	
	Pre-HILDCAA	HILDCAA	Pre-HILDCAA	HILDCAA	Pre-HILDCAA	HILDCAA
P_{FAC0} (Value ± Standard Error)	0.16 ± 0.08	0.10 ± 0.05	0.13 ± 0.09	0.07 ± 0.06	0.09 ± 0.09	0.06 ± 0.05
$x_{c\mathrm{FAC}}$ (Value ± Standard Error)	1.93 ± 0.05	4.71 ± 0.06	1.13 ± 0.02	2.54 ± 0.03	0.82 ± 0.04	2.19 ± 0.03
w_{FAC} (Value ± Standard Error)	2.15 ± 0.10	4.10 ± 0.14	1.11 ± 0.04	2.18 ± 0.07	1.62 ± 0.09	2.24 ± 0.07
A_{FAC} (Value ± Standard Error)	22.09 ± 0.93	23.03 ± 0.84	22.51 ± 0.79	23.57 ± 0.71	27.11 ± 1.23	24.19 ± 0.65
X^2	0.44	0.14	0.71	0.26	0.61	0.21
r	0.96	0.97	0.97	0.98	0.97	0.98

time FAC intensity distributions for different seasons are shown in Figures 2d–2f, and corresponding statistical parameters are listed in Table 1.

Considering quiet time (HILDCAA-related) distributions, FAC_{total} (Figure 2d, Table 1) exhibits 1-σ deviations of ~78%, 55%, 88%, and 75% (~48%, 43%, 50%, and 57%) from corresponding mean intensities during spring, summer, fall, and winter seasons, respectively. The deviations are ~72%, 53%, 93%, and 72% (~51%, 44%, 52%, and 57%) for FAC_{day} (Figure 2e, Table 1), and ~100%, 67%, 93%, and 89% (~54%, 50%, 54%, and 63%) for FAC_{night} (Figure 2f, Table 1), respectively, for quiet time (HILDCAA-related) FAC intensity distributions. Thus, HILDCAA-related FAC intensity distributions are characterized by smaller deviations (from corresponding mean intensities) compared to those during quiet intervals.

Statistical significance of the results presented in Figures 2d–2f and Table 1 are verified through computations of statistical probability factor p. The p-values are listed and inferences are summarized in Table 4. Statistical differences in FAC intensities among different seasons, and between HILDCAAs and quiet times are found to be statistically significant (confirmed by p-values less than 0.05). In general, FAC intensities are prominently stronger during HILDCAAs compared to their quiet time values in all seasons. Quiet time FAC intensity is the strongest in the summer hemisphere (both dayside and nightside), while the weakest FAC intensity is recorded in the winter hemisphere for dayside FACs, and in the spring hemisphere for nightside FACs. On the other hand, HILDCAA-related FAC intensity is the weakest in the winter hemisphere (both dayside and nightside), while it is the strongest in the summer hemisphere for dayside FACs, and in the fall hemisphere for nightside FACs.

The day-night asymmetry in the FAC intensity variations is further explored by the "double superposed epoch analyses" (Figure 3) for HILDCAAs occurring during northern hemispheric spring (with mean duration of ~2.80 days), summer (~2.90 days), fall (~2.84 days), and winter (~3.18 days). While mean nightside FAC intensities are little stronger than their dayside values during winter (Figure 3d), and are weaker during spring (Figure 3a) and fall (Figure 3c) seasons, the strongest day-night asymmetry is recorded during summer (Figure 3b). Mean dayside FAC intensities are ~0.5–0.7 MA stronger than the nightside FAC intensities both during HILDCAAs and quiet times in the summer hemisphere. However, it may be noted that the day-night differences in all seasons fall within 1-σ deviations, indicating high uncertainties in these results. In other words, in any particular hemisphere (season), there is no statistically significant day-night asymmetry.

4. Summary and Discussions

We conducted a statistical study on seasonal variation of HILDCAA-related FAC intensities in comparison to that of pre-HILDCAA (quiet time) FACs. The study involves 42 HILDCAAs occurring during 2009 through 2023. The main findings are summarized below. All these results are confirmed by statistical significance tests.

1. Intensity of total FACs flowing in both hemispheres during HILDCAAs exhibits an asymmetric Gauss distribution (Table 3), with a median FAC intensity of ~5 MA for all HILDCAAs (Figure 2a, Table 1). This is ~2 times the quiet time median FAC intensity, with slight variations between day and night (Figures 2b and 2c, Tables 1 and 2), and from one season to the other (Figures 2d–2f, Tables 1 and 4).
2. Total FAC intensity flowing in two hemispheres (i.e., FAC without seasonal influence) exhibits statistically significant day-night asymmetry (confirmed by statistical probability factor $p < 0.05$). HILDCAA-related (pre-HILDCAA) FAC intensity is ~15% (~20%) stronger in the dayside than in the nightside (Figures 2b and 2c, Tables 1 and 2). However, when currents flowing in a particular hemisphere (season) is considered, there is no significant day-night asymmetry (Figure 3). These results may imply that seasonal influence dominates over day-night variation of the FAC intensity.
3. During HILDCAAs, the dayside FAC intensity is found to be the strongest during summer, and the summer FAC intensity is ~15%, ~32%, and ~87% stronger than during fall, spring, and winter, respectively (Figure 2e, Tables 1 and 4). The nightside FAC intensity during fall is found to be ~8%, ~10%, and ~29% stronger than during summer, spring, and winter, respectively (Figure 2f, Tables 1 and 4).
4. During pre-HILDCAA (quiet) times, the dayside FAC intensity is found to be the strongest during summer, ~92%, ~96%, and ~128% stronger than during spring, fall, and winter, respectively (Figure 2e, Tables 1 and 4). The nightside FAC intensity during summer is ~51%, ~62%, and ~94% stronger than during fall, winter, and spring, respectively (Figure 2f, Tables 1 and 4).

Table 4
Statistical p-Values Based on Seasonal FAC Intensity Comparisons Shown in Figures 2d–2f and Table 1

		p-value	Inference[a]
Spring versus summer	Pre-HILDCAA	0.00e + 00 0.00e + 00 0.00e + 00	Total, dayside and nightside FAC intensities are ~91, ~92, and ~94% stronger during summer than during spring, respectively.
	HILDCAA	0.00e + 00 0.00e + 00 5.56e − 15	Total, dayside and nightside FAC intensities are ~17, ~32, and ~3% stronger during summer than during spring, respectively.
Spring versus fall	Pre-HILDCAA	5.55e − 19 0.000124 1.29e − 65	Total and nightside (dayside) FAC intensities are ~15, and ~29% (~2%) stronger (weaker) during fall than during spring, respectively.
	HILDCAA	1.44e − 234 1.19e − 280 9.03e − 148	Total, dayside and nightside FAC intensities are ~13, ~15, and ~10% stronger during fall than during spring, respectively.
Spring versus winter	Pre-HILDCAA	3.50e − 10 4.12e − 162 7.39e − 40	Total and dayside (nightside) FAC intensities are ~1, and ~19% (~20%) stronger (weaker) during spring than during winter, respectively.
	HILDCAA	0.00e + 00 0.00e + 00 0.00e + 00	Total, dayside and nightside FAC intensities are ~29, ~42, and ~17% stronger during spring than during winter, respectively.
Summer versus fall	Pre-HILDCAA	0.00e + 00 0.00e + 00 0.00e + 00	Total, dayside and nightside FAC intensities are ~65, ~96, and ~51% stronger during summer than during fall, respectively.
	HILDCAA	2.70e − 48 0.00e + 00 5.24e − 91	Total, and dayside (nightside) FAC intensities are ~4, and ~15% (~8%) stronger (weaker) during summer than during fall, respectively.
Summer versus winter	Pre-HILDCAA	0.00e + 00 0.00e + 00 0.00e + 00	Total, dayside and nightside FAC intensities are ~93, ~128, and ~62% stronger during summer than during winter, respectively.
	HILDCAA	0.00e + 00 0.00e + 00 0.00e + 00	Total, dayside and nightside FAC intensities are ~51, ~87, and ~20% stronger during summer than during winter, respectively.
Fall versus winter	Pre-HILDCAA	4.62e − 12 3.22e − 104 0.001401	Total, dayside and nightside FAC intensities are ~17, ~16, and ~7% stronger during fall than during winter, respectively.
	HILDCAA	0.00e + 00 0.00e + 00 0.00e + 00	Total, dayside and nightside FAC intensities are ~46, ~63, and ~29% stronger during fall than during winter, respectively.
Pre-HILDCAA versus HILDCAA	Spring	0.00e + 00 0.00e + 00 0.00e + 00	Total, dayside and nightside FAC intensities are ~189, ~153, and ~234% (by factors of ~2.9, ~2.5, and ~3.3) stronger during HILDCAAs than quiet periods, respectively.
	Summer	0.00e + 00 0.00e + 00 0.00e + 00	Total, dayside and nightside FAC intensities are ~78, ~73, and ~76% (by factors of ~1.8, ~1.7, and ~1.8) stronger during HILDCAAs than quiet periods, respectively.
	Fall	0.00e + 00 0.00e + 00 0.00e + 00	Total, dayside and nightside FAC intensities are ~184, ~196, and ~187% (by factors of ~2.8, ~3.0, and ~2.9) stronger during HILDCAAs than quiet periods, respectively.
	Winter	0.00e + 00 0.00e + 00 0.00e + 00	Total, dayside and nightside FAC intensities are ~127, ~112, and ~138% (by factors of ~2.3, ~2.1, and ~2.4) stronger during HILDCAAs than quiet periods, respectively.

Note. Three p-values in each row correspond to FAC_{total}, FAC_{day}, and FAC_{night}, respectively. A p-value less than 0.05 ($p < 0.05$) indicates statistically significant differences in median values between the two comparing events such as day and night or pre-HILDCAA and HILDCAA intervals. [a]The percentages are based on mean values listed in Table 1.

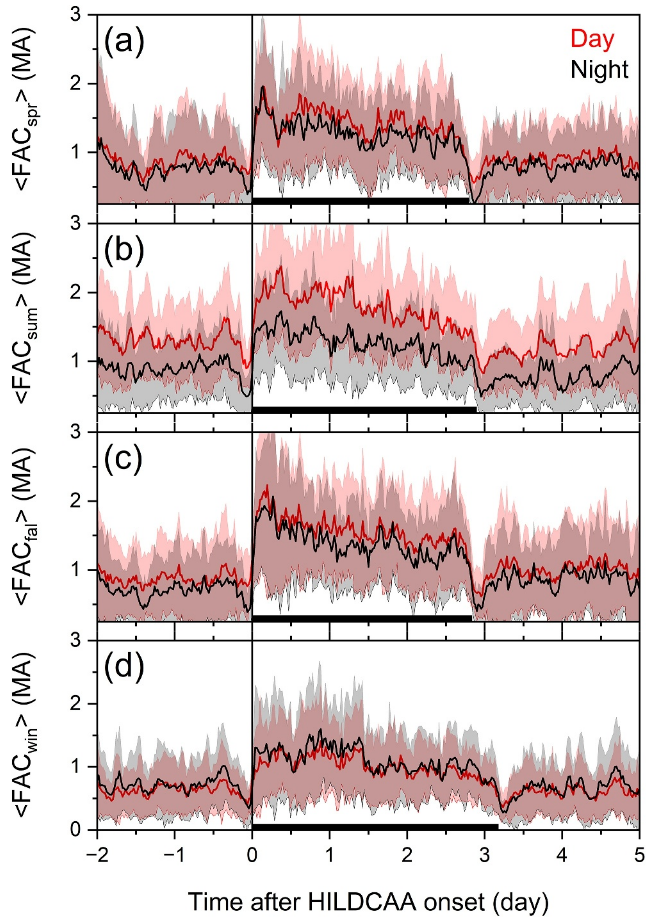

Figure 3. Superposed epoch mean variations of dayside (red) and nightside (black) FAC intensities for (a) spring, (b) summer, (c) fall, and (d) winter hemispheres. Shadings represent 1-σ deviations from the mean intensities. The zero epoch time corresponds to the HILDCAA onset time (marked by a vertical line). The mean durations of HILDCAAs during different seasons are marked by horizontal bars at the bottom of each panel.

Intensification of the FAC intensity during HILDCAAs compared to pre-HILDCAA quiet interval, as shown through case (Figure 1) and statistical (Figures 2 and 3) studies here, reflects the well-established relationship between FAC intensity and geomagnetic activity indices (e.g., Coxon et al., 2014; Forsyth et al., 2018; Hajra et al., 2025a; Knipp et al., 2014; Pedersen et al., 2021, 2022; Wang et al., 2024; Wilder et al., 2012, and references therein). However, previous studies involved geomagnetic storms and substorms, both of which have significantly different magnetospheric convection electric fields than for the HILDCAAs (e.g., Gonzalez et al., 1994). HILDCAAs represent long intervals (2 days to weeks) of substorms/convection events (Guarnieri et al., 2018; Hajra et al., 2013; Kozyra et al., 2006; Mendes et al., 2017; Souza et al., 2016, 2018; Tsurutani et al., 1995; Turner et al., 2006), leading to enhanced energetic particle precipitations in the auroral ionosphere, but only weak ring current activity well below a geomagnetic storm threshold (Gonzalez et al., 1994). Geomagnetic storms are associated with intense and long-duration (a few hours to a day) magnetospheric convection electric fields bringing the ring current closer to the Earth; and modest levels of brief (of the order of a few minutes) convection electric fields may cause substorms. HILDCAAs, on the other hand, are associated with intense and discrete convection electric fields repeating for days to weeks (see Gonzalez et al., 1994 for a comparison of storms, substorms, and HILDCAAs). HILDCAAs are caused by magnetic reconnection (Dungey, 1961) between geomagnetic (northward) fields and IMF southward components of Alfvén waves (Tsurutani & Gonzalez, 1987) carried by solar wind HSSs emanated from coronal holes. Consequent enhanced convections and energetic particle injection lead to FAC intensification. See Hajra et al. (2025b) for a detail discussion of underlying solar wind-magnetosphere-ionosphere coupling leading to FAC intensification during HILDCAAs. It is interesting to note that the HILDCAA-related FAC intensification is intermediate in intensity compared to weaker (~1 MA) FAC intensification during isolated substorms and stronger (~10 times) intensification during intense storms.

Lack of any statistically significant day-night asymmetry in FAC intensity during HILDCAAs is interesting. While dayside FAC intensity is ~0.5–0.7 MA stronger than the nightside FAC intensity in the summer hemisphere (with high 1-σ deviations indicating significant uncertainties in this result), there is no statistically significant day-night asymmetry during any season. Wang et al. (2005), based on 2 years of the Challenging Minisatellite Payload magnetic field data, reported a 2-factor enhancement of the FAC densities for sunlit compared with darkness. The dayside enhancement was attributed to the solar illumination-induced ionospheric conductivity. However, long-duration and almost continuous energetic particle precipitation associated with HILDCAA-related long-duration and intense substorms (e.g., Søraas et al., 2004) may enhance the auroral ionospheric Hall conductance at night (Wang et al., 2024; Wang & Lühr, 2023; Zhong et al., 2022), possibly contributing to enhanced nightside FACs. This may explain lack of any day-night FAC asymmetry during HILDCAAs.

Most interesting results of this work are seasonal dependences of both dayside and nightside FAC intensities during HILDCAAs and pre-HILDCAA quiet intervals. In particular, seasonal dependences of nightside FACs, confirmed by statistical significance test, clearly contradict previous results for FACs during quiet intervals, geomagnetic storms, and substorms. Fujii et al. (1981) and Coxon et al. (2016) reported a summer-winter asymmetry in the dayside FACs, dayside FAC intensities being stronger during summer than during winter by a factor of ~2. However, nightside FAC intensities did not show any significant differences from summer to winter. Anderson et al. (2002) observed similar global dayside FAC intensifications and temporal developments in both the southern spring and northern fall hemispheres during two intense geomagnetic storms with Dst intensities of −160 and −230 nT. Wang et al. (2006) studied FAC variations associated with four intense storms with Dst intensities of −180, −363, −401, and −472 nT occurring during October and November 2003, and concluded that dayside FAC densities were 2.5 times higher, on average, in the summer hemisphere compared to the winter hemisphere, while nightside intensities were comparable in both hemispheres. In summary, previous studies reported (a) summer-winter asymmetry in dayside FAC intensity, (b) no summer-winter asymmetry in nightside FAC intensity, and (c) no spring-fall asymmetry in FAC intensities. These results are based on limited numbers of case studies during geomagnetic storms (e.g., Anderson et al., 2002; Wang et al., 2006) or on quiet time statistical studies based on limited FAC observations (e.g., Coxon et al., 2016; Fujii et al., 1981). More recently, Hajra et al. (2025a) explored ~15 years of AMPERE FAC measurements, and reported that the dayside FAC intensity in the summer hemisphere is ~99% stronger than in the winter hemisphere, and ~35%−38% stronger than in equinoxes. The nightside FAC intensity in winter is found to be ~14%–17% weaker than in other seasons. In addition, these seasonal features are found to be consistent across all years and levels of solar activity. Present results of seasonal dependences of both dayside and nightside FAC intensities seem to be consistent with Hajra et al. (2025a) results, but for HILDCAAs and pre-HILDCAA intervals.

Seasonal variations of dayside FAC intensities have been explained by Wang et al. (2005, 2006, 2024) as being related to stronger (weaker) ionospheric conductance caused by higher (lower) rate of photoionization or higher (lower) solar illumination of the summer (winter) hemisphere. How to explain seasonal variations of nightside FAC intensities? Hajra et al. (2025a) showed that while dayside FACs are largely controlled by ionospheric conductance, nightside FACs with lesser influence of ionospheric conductance are strongly correlated to the solar wind-magnetosphere energy coupling processes. Thus, further studies on the possible seasonal dependences of the coupling and consequent magnetospheric convections are required to understand the seasonal variations of nightside FAC intensities.

Appendix A: Mann Whitney Wilcoxon Test/Wilcoxon Rank Sum Test

The Mann Whitney Wilcox test/Mann Whitney U test/Wilcoxon rank-sum test is a non-parametric test used to compare two independent groups. It does not assume normality. Instead, it compares the ranks of the data. It is assumed that the two samples are independent. If distributions are similar in shape, the test is often interpreted as comparing medians.

To estimate the test statistic U, data from both groups are combined and ranks are assigned to them. If sums of ranks of the groups 1 and 2 are $R1$ and $R2$, respectively, and sizes of the groups are $n1$ and $n2$, respectively,

$$U1 = n1n2 + \frac{n1(n1+1)}{2} - R1$$

$$U2 = n1n2 + \frac{n2(n2+1)}{2} - R2$$

$$U = \min(U1, U2)$$

Null hypothesis (H0) is that the two groups come from the same distribution, the alternative hypothesis (H1) is that one group tends to have larger/smaller values than the other.

In this test, all data points from both groups are ranked together, from the smallest to the largest values. Once all values are ranked, the sums of the ranks from each group are computed. Thus, if the two groups come from identical populations, then the rank sums for both groups are expected to be roughly equal. In other words, significant deviations from this expectation can indicate differences between the groups.

Under the null hypothesis (i.e., both groups come from the same distribution), the expected value of U is:

$$E(U) = \frac{n1n2}{2}$$

The variance of U is:

$$\mathrm{var}(U) = \frac{n1n2(n1+n2+1)}{12}$$

Under the null hypothesis, and with large enough sample sizes, U is approximately normally distributed. This property allows us to standardize U and compare it to a standard normal distribution to determine its significance. The standardized test statistic, Z, is given by:

$$Z = \frac{U - E(U)}{\sqrt{\mathrm{var}(U)}}$$

The value of Z can then be used to determine the p-value and test the hypothesis. A significant p-value (typically <0.05) indicates that the distributions of the two groups are not the same.

For example, for pre-HILDCAA FAC (HILDCAA-related dayside FAC) intensity distributions, U statistic is 330799349 (898294933.5), sample sizes for dayside and nightside FAC data (spring and summer hemispheric FAC intensity) are 29673 and 27705 (39804 and 46570), respectively; sums of their ranks are 931549417 and 714596714 (1690494043.5 and 2039783081.5), respectively, and the estimated two-tailed p-value at the significance level of 0.05 is 0.00e + 00 (5.56e−15).

Appendix B: Gaussian Curve Fitting

The FAC intensity distributions presented in Figures 2a–2c are fitted to a Gauss distribution function using the Levenberg Marquardt iteration algorithm. The functional form is as follows:

$$y = y_0 + \frac{A}{w\sqrt{\frac{\pi}{2}}} e^{-2\left(\frac{x-x_c}{w}\right)^2}$$

The parameters are defined in Figure B1: y_0 is the "offset", x_c is the "center", w is the "width", and A is the "area."

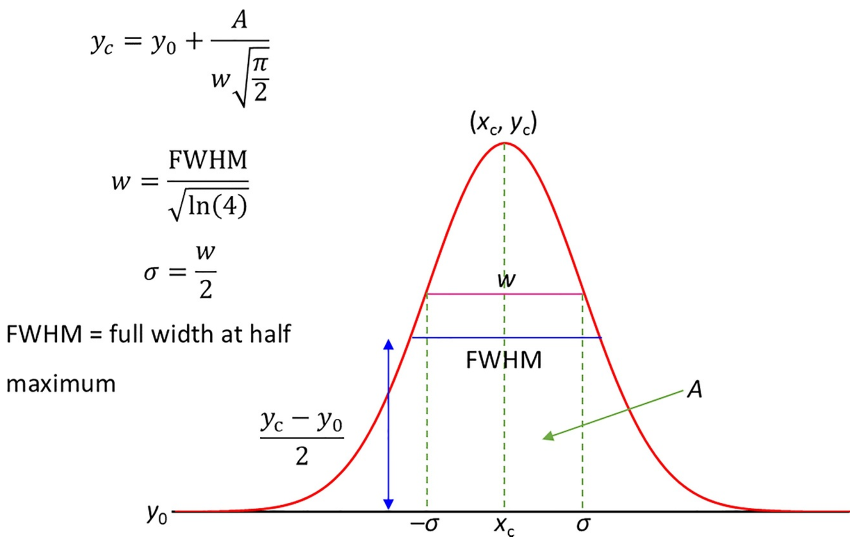

Figure B1. Gaussian curve fitting.

Conflict of Interest

The authors declare no conflicts of interest relevant to this study.

Data Availability Statement

The FAC data are obtained from the AMPERE Science Data Center of the Johns Hopkins Applied Physics Laboratory (https://ampere.jhuapl.edu/). The data is free to download from the download page under the AMPERE Derived Product Data Files (Daily) (https://ampere.jhuapl.edu/download/?page=derivedProductsTab). The near-Earth solar wind plasma and IMF data are obtained from NASA's OMNIWeb Plus database (https://omniweb.gsfc.nasa.gov/). The high-resolution data can be directly downloaded from the page: https://omniweb.gsfc.nasa.gov/form/omni_min.html, by specifying start and stop times. The geomagnetic Dst, AE, and SYM-H indices are obtained from the World Data Center for Geomagnetism, Kyoto, Japan (https://wdc.kugi.kyoto-u.ac.jp/). Specific index can be freely downloaded from the Data Service page (https://wdc.kugi.kyoto-u.ac.jp/wdc/Sec3.html) by selecting the index and then specifying start and end times. The SME, SMU, and SML indices are obtained from the SuperMAG database (https://supermag.jhuapl.edu/). The indices are freely available to plot and download through the Indices page (https://supermag.jhuapl.edu/indices/?fidelity=low&layers=SME.UL&start=2001-01-29T16%3A00%3A00.000Z&step=14400&tab=plot) by specifying time, duration and selecting the indices.

Acknowledgments
The work of R. H. is funded by the "Hundred Talents Program" of the Chinese Academy of Sciences (CAS), and the "Excellent Young Scientists Fund Program (Overseas)" of the National Natural Science Foundation of China (NSFC). We would like to thank the reviewers for extremely valuable suggestions that substantially improved the manuscript.

References

Alfvén, H. (1942). Existence of electromagnetic-hydrodynamic waves. *Nature*, *150*(3805), 405–406. https://doi.org/10.1038/150405d0

Anderson, B. J., Angappan, R., Barik, A., Vines, S. K., Stanley, S., Bernasconi, P. N., et al. (2021). Iridium communications satellite constellation data for study of Earth's magnetic field. *Geochemistry, Geophysics, Geosystems*, *22*(8), e2020GC009515. https://doi.org/10.1029/2020GC009515

Anderson, B. J., Korth, H., Waters, C. L., Green, D. L., Merkin, V. G., Barnes, R. J., & Dyrud, L. P. (2014). Development of large-scale Birkeland currents determined from the active magnetosphere and planetary electrodynamics response experiment. *Geophysical Research Letters*, *41*(9), 3017–3025. https://doi.org/10.1002/2014GL059941

Anderson, B. J., Takahashi, K., Kamei, T., Waters, C. L., & Toth, B. A. (2002). Birkeland current system key parameters derived from iridium observations: Method and initial validation results. *Journal of Geophysical Research*, *107*(A6), SMP11-1–SMP11-13. https://doi.org/10.1029/2001JA000080

Baker, K. B., & Wing, S. (1989). A new magnetic coordinate system for conjugate studies at high latitudes. *Journal of Geophysical Research*, *94*(A7), 9139–9143. https://doi.org/10.1029/JA094iA07p09139

Belcher, J. W., & Davis, L., Jr. (1971). Large-amplitude Alfvén waves in the interplanetary medium, 2. *Journal of Geophysical Research*, *76*(16), 3534–3563. https://doi.org/10.1029/JA076i016p03534

Birkeland, K. (1908). *The Norwegian Aurora polaris expedition 1902–1903* (Vol. 1). H. Aschelhoug and Company.

Birkeland, K. (1913). *The Norwegian Aurora polaris expedition 1902–1903* (Vol. 2). H. Aschelhoug and Company.

Cheng, Z. W., Shi, J. K., Zhang, J. C., Torkar, K., Kistler, L. M., Dunlop, M., et al. (2018). Influence of the IMF cone angle on invariant latitudes of polar region footprints of FACs in the magnetotail: Cluster observation. *Journal of Geophysical Research: Space Physics*, *123*(4), 2588–2597. https://doi.org/10.1002/2017JA024941

Clausen, L. B. N., Baker, J. B. H., Ruohoniemi, J. M., Milan, S. E., & Anderson, B. J. (2012). Dynamics of the region 1 Birkeland current oval derived from the active magnetosphere and planetary electrodynamics response experiment (AMPERE). *Journal of Geophysical Research*, *117*(A6), A06233. https://doi.org/10.1029/2012JA017666

Coleman, P. J. (1966). Hydromagnetic waves in the interplanetary plasma. *Physical Review Letters*, *17*(4), 207–211. https://doi.org/10.1103/PhysRevLett.17.207

Cowley, S. W. H. (2000). Magnetosphere-ionosphere interactions: A tutorial review. In S.-I. Ohtani, R. Fujii, M. Hesse, & R. L. Lysak (Eds.), *Magnetospheric current systems*. https://doi.org/10.1029/GM118p0091

Coxon, J. C., Milan, S. E., Carter, J. A., Clausen, L. B. N., Anderson, B. J., & Korth, H. (2016). Seasonal and diurnal variations in AMPERE observations of the Birkeland currents compared to modeled results. *Journal of Geophysical Research: Space Physics*, *121*(5), 4027–4040. https://doi.org/10.1002/2015JA022050

Coxon, J. C., Milan, S. E., Clausen, L. B. N., Anderson, B. J., & Korth, H. (2014). A superposed epoch analysis of the regions 1 and 2 Birkeland currents observed by AMPERE during substorms. *Journal of Geophysical Research: Space Physics*, *119*(12), 9834–9846. https://doi.org/10.1002/2014JA020500

Dessler, A. J., & Parker, E. N. (1959). Hydromagnetic theory of geomagnetic storms. *Journal of Geophysical Research*, *64*(12), 2239–2252. https://doi.org/10.1029/JZ064i012p02239

Dungey, J. W. (1961). Interplanetary magnetic field and the auroral zones. *Physical Review Letters*, *6*(2), 47–48. https://doi.org/10.1103/PhysRevLett.6.47

Forsyth, C., Shortt, M., Coxon, J. C., Rae, I. J., Freeman, M. P., Kalmoni, N. M. E., et al. (2018). Seasonal and temporal variations of field-aligned currents and ground magnetic deflections during substorms. *Journal of Geophysical Research: Space Physics*, *123*(4), 2696–2713. https://doi.org/10.1002/2017JA025136

Fujii, R., Iijima, T., Potemra, T. A., & Sugiura, M. (1981). Seasonal dependence of large-scale Birkeland currents. *Geophysical Research Letters*, *8*(10), 1103–1106. https://doi.org/10.1029/GL008i010p01103

Gibbons, J. D., & Chakraborti, S. (2011). Nonparametric statistical inference. In M. Lovric (Ed.), *International encyclopedia of statistical science* (pp. 977–979). Springer. https://doi.org/10.1007/978-3-642-04898-2_420

Gjerloev, J. (2009). A global ground-based magnetometer initiative. *Eos, Transactions American Geophysical Union*, *90*(27), 230–231. https://doi.org/10.1029/2009EO270002

Gjerloev, J. (2012). The SuperMAG data processing technique. *Journal of Geophysical Research*, *117*(A9), A09213. https://doi.org/10.1029/2012JA017683

Gonzalez, W. D., Joselyn, J. A., Kamide, Y., Kroehl, H. W., Rostoker, G., Tsurutani, B. T., & Vasyliunas, V. M. (1994). What is a geomagnetic storm? *Journal of Geophysical Research*, *99*(A4), 5771–5792. https://doi.org/10.1029/93JA02867

Guarnieri, F. L., Tsurutani, B. T., Vieira, L. E. A., Hajra, R., Echer, E., Mannucci, A. J., & Gonzalez, W. D. (2018). A correlation study regarding the AE index and ACE solar wind data for Alfvénic intervals using wavelet decomposition and reconstruction. *Nonlinear Processes in Geophysics*, *25*(1), 67–76. https://doi.org/10.5194/npg-25-67-2018

Hajra, R. (2021). 2017 space-weather events: A study on magnetic reconnection and geoeffectiveness. *Solar Physics*, *296*(3), 50. https://doi.org/10.1007/s11207-021-01803-7

Hajra, R., Echer, E., Franco, A. M. S., & Bolzan, M. J. A. (2023). Earth's magnetotail variability during supersubstorms (SSSs): A study on solar wind–magnetosphere–ionosphere coupling. *Advances in Space Research*, *72*(4), 1208–1223. https://doi.org/10.1016/j.asr.2023.04.013

Hajra, R., Echer, E., Tsurutani, B. T., & Gonzalez, W. D. (2013). Solar cycle dependence of high-intensity long-duration continuous AE activity (HILDCAA) events, relativistic electron predictors? *Journal of Geophysical Research: Space Physics*, *118*(9), 5626–5638. https://doi.org/10.1002/jgra.50530

Hajra, R., Echer, E., Tsurutani, B. T., & Gonzalez, W. D. (2014a). Superposed epoch analyses of HILDCAAs and their interplanetary drivers: Solar cycle and seasonal dependences. *Journal of Atmospheric and Solar-Terrestrial Physics*, *121*(A), 24–31. https://doi.org/10.1016/j.jastp.2014.09.012

Hajra, R., Echer, E., Tsurutani, B. T., & Gonzalez, W. D. (2014b). Solar wind-magnetosphere energy coupling efficiency and partitioning: HILDCAAs and preceding CIR storms during solar cycle 23. *Journal of Geophysical Research: Space Physics*, *119*(4), 2675–2690. https://doi.org/10.1002/2013JA019646

Hajra, R., & Tsurutani, B. T. (2018). Interplanetary shocks inducing magnetospheric supersubstorms (SML < -2500 nT): Unusual auroral morphologies and energy flow. *The Astrophysical Journal*, *858*(2), 123. https://doi.org/10.3847/1538-4357/aabaed

Hajra, R., Tsurutani, B. T., Echer, E., & Gonzalez, W. D. (2014c). Relativistic electron acceleration during high-intensity, long-duration, continuous AE activity (HILDCAA) events: Solar cycle phase dependences. *Geophysical Research Letters*, *41*(6), 1876–1881. https://doi.org/10.1002/2014GL05938

Hajra, R., Tsurutani, B. T., Echer, E., Gonzalez, W. D., Brum, C. G. M., Vieira, L. E. A., & Santolik, O. (2015). Relativistic electron acceleration during HILDCAA events: Are precursor CIR magnetic storms important? *Earth Planets and Space*, *67*(1), 109. https://doi.org/10.1186/s40623-015-0280-5

Hajra, R., Tsurutani, B. T., Echer, E., Gonzalez, W. D., & Gjerloev, J. W. (2016). Supersubstorms (SML < -2500 nT): Magnetic storm and solar cycle dependences. *Journal of Geophysical Research: Space Physics*, *121*(8), 7805–7816. https://doi.org/10.1002/2015JA021835

Hajra, R., Tsurutani, B. T., Echer, E., Gonzalez, W. D., & Santolik, O. (2015). Relativistic ($E > 0.6$, > 2.0, and > 4.0 MeV) electron acceleration at geosynchronous orbit during high-intensity, long-duration, continuous AE activity (HILDCAA) events. *The Astrophysical Journal*, *799*(1), 39. https://doi.org/10.1088/0004-637X/799/1/39

Hajra, R., Tsurutani, B. T., & Lakhina, G. S. (2020). The complex space weather events of 2017 September. *The Astrophysical Journal*, *899*(1), 3. https://doi.org/10.3847/1538-4357/aba2c5

Hajra, R., Tsurutani, B. T., Lakhina, G. S., Lu, Q., & Du, A. (2024). Interplanetary causes and impacts of the 2024 may superstorm on the geosphere: An overview. *The Astrophysical Journal*, *974*(2), 264. https://doi.org/10.3847/1538-4357/ad7462

Hajra, R., Tsurutani, B. T., Lu, Q., Du, A., Lu, S., & Echer, E. (2025a). Solar cycle and seasonal dependences of field-aligned currents. *Space Weather*, *23*(5), e2025SW004441. https://doi.org/10.1029/2025SW004441

Hajra, R., Tsurutani, B. T., Lu, Q., Du, A., Lu, S., & Gao, X. (2025b). Field-aligned currents during high-intensity long-duration continuous auroral electrojet activity events: A statistical study. *Space Weather*, *23*, e2025SW004353. https://doi.org/10.1029/2025SW004353

Hajra, R., Tsurutani, B. T., Lu, Q., Horne, R. B., Lakhina, G. S., Yang, X., et al. (2024). The April 2023 SYM-H $= -233$ nT geomagnetic storm: A classical event. *Journal of Geophysical Research: Space Physics*, *129*(10), e2024JA032986. https://doi.org/10.1029/2024JA032986

Hajra, R., Tsurutani, B. T., Lu, Q., Lakhina, G. S., Du, A., Echer, E., et al. (2024). Ultra-relativistic electron acceleration during high-intensity long-duration continuous auroral electrojet activity events. *The Astrophysical Journal*, *965*(2), 146. https://doi.org/10.3847/1538-4357/ad2dfe

Iijima, T., & Potemra, T. A. (1978). Large-scale characteristics of field-aligned currents associated with substorms. *Journal of Geophysical Research*, *83*(A2), 599–615. https://doi.org/10.1029/JA083iA02p00599
Iijima, T., & Potemra, T. A. (1976). Field-aligned currents in the dayside cusp observed by triad. *Journal of Geophysical Research*, *81*(34), 5971–5979. https://doi.org/10.1029/JA081i034p05971
Iyemori, T. (1990). Storm-time magnetospheric currents inferred from mid-latitutde geomagnetic field variations. *Journal of Geomagnetism and Geoelectricity*, *42*(11), 1249–1265. https://doi.org/10.5636/jgg.42.1249
Käki, S., Viljanen, A., Juusola, L., & Kauristie, K. (2022). Spatio-temporal development of large-scale auroral electrojet currents relative to substorm onsets. *Annales Geophysicae*, *40*(1), 107–119. https://doi.org/10.5194/angeo-40-107-2022
King, J. H., & Papitashvili, N. E. (2020). OMNI 1-min data set [Dataset]. *NASA Space Physics Data Facility*. https://doi.org/10.48322/45BB-8792
Knipp, D. J., Matsuo, T., Kilcommons, L., Richmond, A., Anderson, B., Korth, H., et al. (2014). Comparison of magnetic perturbation data from LEO satellite constellations: Statistics of DMSP and AMPERE. *Space Weather*, *12*(1), 2–23. https://doi.org/10.1002/2013SW000987
Kozyra, J. U., Crowley, G., Emery, B. A., Fang, X., Maris, G., Mlynczak, M. G., et al. (2006). Response of the upper/middle atmosphere to coronal holes and powerful high-speed solar wind streams in 2003. In B. T. Tsurutani, R. McPherron, G. Lu, J. H. A. Sobral, & N. Gopalswamy (Eds.), *Recurrent magnetic storms: Corotating solar wind streams*. https://doi.org/10.1029/167GM24
Krieger, A., Timothy, A., & Roelof, E. (1973). A coronal hole and its identification as the source of a high velocity solar wind stream. *Solar Physics*, *29*(2), 505–525. https://doi.org/10.1007/BF00150828
Laundal, K. M., Finlay, C. C., Olsen, N., & Reistad, J. P. (2018). Solar wind and seasonal influence on ionospheric currents from swarm and CHAMP measurements. *Journal of Geophysical Research: Space Physics*, *123*(5), 4402–4429. https://doi.org/10.1029/2018JA025387
Le, G., Lühr, H., Anderson, B. J., Strangeway, R. J., Russell, C. T., Singer, H., et al. (2016). Magnetopause erosion during the 17 march 2015 magnetic storm: Combined field-aligned currents, auroral oval, and magnetopause observations. *Geophysical Research Letters*, *43*(6), 2396–2404. https://doi.org/10.1002/2016GL068257
Lyons, L. R., Gallardo-Lacourt, B., Zou, S., Weygand, J. M., Nishimura, Y., Li, W., et al. (2016). The 17 March 2013 storm: Synergy of observations related to electric field modes and their ionospheric and magnetospheric effects. *Journal of Geophysical Research: Space Physics*, *121*(11), 10880–10897. https://doi.org/10.1002/2016JA023237
Mendes, O., Domingues, M. O., Echer, E., Hajra, R., & Menconi, V. E. (2017). Characterization of high-intensity, long-duration continuous auroral activity (HILDCAA) events using recurrence quantification analysis. *Nonlinear Processes in Geophysics*, *24*(3), 407–417. https://doi.org/10.5194/npg-24-407-2017
Neugebauer, M., Clay, D. R., Goldstein, B. E., Tsurutani, B. T., & Zwickl, R. D. (1984). A reexamination of rotational and tangential discontinuities in the solar wind. *Journal of Geophysical Research*, *89*(A7), 5395–5408. https://doi.org/10.1029/JA089iA07p05395
Neugebauer, M., & Snyder, C. W. (1966). Mariner 2 observations of the solar wind: 1. Average properties. *Journal of Geophysical Research*, *71*(19), 4469–4484. https://doi.org/10.1029/JZ071i019p04469
Newell, P., & Gjerloev, J. (2011a). Evaluation of SuperMAG auroral electrojet indices as indicators of substorms and auroral power. *Journal of Geophysical Research*, *116*(A12), A12211. https://doi.org/10.1029/2011JA016779
Newell, P., & Gjerloev, J. (2011b). Substorm and magnetosphere characteristic scales inferred from the SuperMAG auroral electrojet indices. *Journal of Geophysical Research*, *116*(A12), A12232. https://doi.org/10.1029/2011JA016936
Pedersen, M. N., Vanhamäki, H., Aikio, A. T., Käki, S., Workayehu, A. B., Waters, C. L., & Gjerloev, J. W. (2021). Field-aligned and ionospheric currents by AMPERE and SuperMAG during HSS/SIR-driven storms. *Journal of Geophysical Research: Space Physics*, *126*(11), e2021JA029437. https://doi.org/10.1029/2021JA029437
Pedersen, M. N., Vanhamäki, H., Aikio, A. T., Waters, C. L., Gjerloev, J. W., Käki, S., & Workayehu, A. B. (2022). Effect of ICME-driven storms on field-aligned and ionospheric currents from AMPERE and SuperMAG. *Journal of Geophysical Research: Space Physics*, *127*(8), e2022JA030423. https://doi.org/10.1029/2022JA030423
Phillips, J. L., Bame, S. J., Feldman, W. C., Gosling, J. T., Hammond, C. M., McComas, D. J., et al. (1995). Ulysses solar wind plasma observations at high southerly Latitudes. *Science*, *268*(5213), 1030–1033. https://doi.org/10.1126/science.268.5213.1030
Press, W. H., Teukolsky, S. A., Vetterling, W. T., & Flannery, B. P. (1992). *Numerical recipes: The art of scientific computing* (2nd ed.). Cambridge University Press.
Qu, B. H., Lu, J. Y., Wang, Z. W., Liu, J. J., Wang, M., Li, J. Y., & Zhang, H. (2024). Estimation of ionospheric field-aligned currents using SuperDARN radar and DMSP observations. *Journal of Geophysical Research: Space Physics*, *129*(6), e2024JA032708. https://doi.org/10.1029/2024ja032708
Reiff, P. H. (1990). The use and misuse of statistics in space physics. *Journal of Geomagnetism and Geoelectricity*, *42*(9), 1145–1174. https://doi.org/10.5636/jgg.42.1145
Rostoker, G. (1972). Geomagnetic indices. *Reviews of Geophysics*, *10*(4), 935–950. https://doi.org/10.1029/RG010i004p00935
Sckopke, N. (1966). A general relation between the energy of trapped particles and the disturbance field near the Earth. *Journal of Geophysical Research*, *71*(13), 3125–3130. https://doi.org/10.1029/JZ071i013p03125
Smith, E. J., & Wolfe, J. H. (1976). Observations of interaction regions and corotating shocks between one and five AU: Pioneers 10 and 11. *Geophysical Research Letters*, *3*(3), 137–140. https://doi.org/10.1029/GL003i003p00137
Søraas, F., Aarsnes, K., Oksavik, K., Sandanger, M. I., Evans, D. S., & Greer, M. S. (2004). Evidence for particle injection as the cause of Dst reduction during HILDCAA events. *Journal of Atmospheric and Solar-Terrestrial Physics*, *66*(2), 177–186. https://doi.org/10.1016/j.jastp.2003.05.001
Souza, A. M., Echer, E., Bolzan, M. J. A., & Hajra, R. (2016). A study on the main periodicities in interplanetary magnetic field Bz component and geomagnetic AE index during HILDCAA events using wavelet analysis. *Journal of Atmospheric and Solar-Terrestrial Physics*, *149*, 81–86. https://doi.org/10.1016/j.jastp.2016.09.006
Souza, A. M., Echer, E., Bolzan, M. J. A., & Hajra, R. (2018). Cross-correlation and cross-wavelet analyses of the solar wind IMF Bz and auroral electrojet index AE coupling during HILDCAAs. *Annales Geophysicae*, *36*(1), 205–211. https://doi.org/10.5194/angeo-36-205-2018
Tsurutani, B. T., & Gonzalez, W. D. (1987). The cause of high-intensity long-duration continuous AE activity (HILDCAAs): Interplanetary Alfvén wave trains. *Planetary and Space Science*, *35*(4), 405–412. https://doi.org/10.1016/0032-0633(87)90097-3
Tsurutani, B. T., Gonzalez, W. D., Gonzalez, A. L. C., Guarnieri, F. L., Gopalswamy, N., Grande, M., et al. (2006). Corotating solar wind streams and recurrent geomagnetic activity: A review. *Journal of Geophysical Research*, *111*(A7), A07S01. https://doi.org/10.1029/2005JA011273
Tsurutani, B. T., Gonzalez, W. D., Gonzalez, A. L. C., Tang, F., Arballo, J. K., & Okada, M. (1995). Interplanetary origin of geomagnetic activity in the declining phase of the solar cycle. *Journal of Geophysical Research*, *100*(A11), 21717–21733. https://doi.org/10.1029/95JA01476
Tsurutani, B. T., & Hajra, R. (2023). Energetics of shock-triggered supersubstorms (SML < -2500 nT). *The Astrophysical Journal*, *946*(1), 17. https://doi.org/10.3847/1538-4357/acb143

Tsurutani, B. T., Hajra, R., Echer, E., & Gjerloev, J. W. (2015). Extremely intense (SML ≤–2500 nT) substorms: Isolated events that are externally triggered? *Annales Geophysicae*, *33*(5), 519–524. https://doi.org/10.5194/angeo-33-519-2015

Turner, N. E., Mitchell, E. J., Knipp, D. J., & Emery, B. A. (2006). Energetics of magnetic storms driven by corotating interaction regions: A study of geoeffectiveness. In B. T. Tsurutani, R. McPherron, G. Lu, J. H. A. Sobral, & N. Gopalswamy (Eds.), *Recurrent magnetic storms: Corotating solar wind streams*. https://doi.org/10.1029/167GM11

Wang, H., Cheng, Q., Lühr, H., Zhong, Y., Zhang, K., & Xia, H. (2024). Local time and hemispheric asymmetries of field-aligned currents and polar electrojet during May 2024 superstorm periods. *Journal of Geophysical Research: Space Physics*, *129*(11), e2024JA033020. https://doi.org/10.1029/2024JA033020

Wang, H., & Lühr, H. (2023). Magnetic longitudinal and local time variations of polar electrojet and field-aligned currents. *Journal of Geophysical Research: Space Physics*, *128*(10), e2023JA031874. https://doi.org/10.1029/2023JA031874

Wang, H., Lühr, H., & Ma, S. Y. (2005). Solar zenith angle and merging electric field control of field-aligned currents: A statistical study of the Southern Hemisphere. *Journal of Geophysical Research*, *110*(A3), 2004JA010530. https://doi.org/10.1029/2004JA010530

Wang, H., Lühr, H., Ma, S. Y., Weygand, J., Skoug, R. M., & Yin, F. (2006). Field-aligned currents observed by CHAMP during the intense 2003 geomagnetic storm events. *Annales Geophysicae*, *24*(1), 311–324. https://doi.org/10.5194/angeo-24-311-2006

Waters, C. L., Anderson, B. J., Green, D. L., Korth, H., Barnes, R. J., & Vanhamäki, H. (2020). Science data products for AMPERE. In M. Dunlop & H. Lühr (Eds.), *Ionospheric multi-spacecraft analysis tools*, *ISSI scientific report series* (Vol. 17, pp. 141–165). Springer. https://doi.org/10.1007/978-3-030-26732-2_7

Waters, C. L., Anderson, B. J., & Liou, K. (2001). Estimation of global field aligned currents using the iridium® system magnetometer data. *Geophysical Research Letters*, *28*(11), 2165–2168. https://doi.org/10.1029/2000GL012725

Wilder, F. D., Crowley, G., Anderson, B. J., & Richmond, A. D. (2012). Intense dayside Joule heating during the 5 April 2010 geomagnetic storm recovery phase observed by AMIE and AMPERE. *Journal of Geophysical Research*, *117*(A5), A05207. https://doi.org/10.1029/2011JA017262

Zhong, Y., Wang, H., Zhang, K., Xia, H., & Qian, C. (2022). Local time response of auroral electrojet during magnetically disturbed periods: DMSP and CHAMP coordinated observations. *Journal of Geophysical Research: Space Physics*, *127*(8), e2022JA030624. https://doi.org/10.1029/2022JA030624

Zmuda, A. J., Martin, J. H., & Heuring, F. T. (1966). Transverse magnetic disturbances at 1100 kilometers in the auroral region. *Journal of Geophysical Research*, *71*(21), 5033–5045. https://doi.org/10.1029/JZ071i021p05033